metals

MDPI

Article

Effect of Ausforming Temperature on the Microstructure of G91 Steel

Javier Vivas *, Carlos Capdevila, José Antonio Jimenez, Miguel Benito-Alfonso and David San-Martin

Centro Nacional de Investigaciones Metalúrgicas (CENIM), Consejo Superior Investigaciones Científicas (CSIC), Avda Gregorio del Amo, 8, E 28040 Madrid, Spain; ccm@cenim.csic.es (C.C.); jimenez@cenim.csic.es (J.A.J.); mba@cenim.csic.es (M.B.-A.); dsm@cenim.csic.es (D.S.-M.)

* Correspondence: jvm@cenim.csic.es; Tel.: +34-91-553-89-00; Fax: +34-91-534-74-25

Received: 18 May 2017; Accepted: 23 June 2017; Published: 27 June 2017

Abstract: The development of thermomechanical treatments (TMT) has a high potential for improving creep-strength in 9Cr-1Mo ferritic/martensitic steel (ASTM T/P91) to operate at temperatures beyond 600 °C. To maximize the number of nanoscale MX precipitates, an ausforming procedure has been used to increase the number of nucleation sites for precipitation inside the martensite lath. Relative to standard heat treatments (consisting of austenitization at about 1040 °C followed by tempering at about 730 °C) this processing concept has enabled achieving a microstructure containing approximately three orders of magnitude higher number density of MX precipitates having a size around four times smaller in ASTM T/P91 steel. On the other hand; this TMT has little effect on the size and number density of $M_{23}C_6$ particles. The optimized microstructure produced by this TMT route proposed is expected to improve the creep strength of this steel.

Keywords: creep resistant steels; carbonitrides precipitation; martensite; tempering; thermomechanical treatment; ferritic/martensitic steel; MX nanoprecipitates

1. Introduction

The 9-12Cr Ferritic/martensitic (FM) steels are widely used in power generating and petrochemical plants for operating temperatures up to 620 °C because of their excellent combination of creep strength, thermal properties, and oxidation resistance as well as acceptable room temperature mechanical properties and also good weldability [1]. In the designs of advanced power plant components for future fission and fusion power plants, which will operate at temperatures up to 650 °C, the primary emphasis was placed on the development of new steel grades with superior long-term creep and thermal fatigue properties [2,3]. Several promising ferritic steels have been developed by the addition of very expensive alloying elements such as W and Co [4–7]. However, there are economic and technical advantages for using the same basic composition of ASTM T/P 91 (here after named G91) and considerably raising creep-strength of this material by the development of thermomechanical treatments (TMT) [8–11]. The creep resistance of a G91 steel results from the combination of several types of barriers to dislocation motion: a high density of martensitic lath boundaries, solid solution strengthening with elements with much larger atomic size than iron, and fine dispersion of second phase particles [12,13]. Although the overall creep strain rate is the result of the combined effects of these mechanisms, it has been reported in previous works that the creep strength is mainly increased by the precipitation of fine MX carbonitrides in the matrix [14,15], which are very effective barriers to pin dislocations, and very stable during long-term aging [16–18].

The goal of this paper is to develop a processing route to improve the creep strength of a conventional G91 steel. Prior to the optimization of TMT, thermodynamic calculations using ThermoCalc® will be carried out to foresee the most promising microstructures. In order to maximize

the number of nanoscale MX precipitates, an ausforming procedure will be applied to increase the number of nucleation sites for precipitation inside the martensite lath relative to standard heat treatments. Previous works have investigated the effect of applying a TMT instead of a conventional heat treatment demonstrating the improvement in creep strength achieved with a finer dispersion of MX [8,9,11]. This work tries to deepen our understanding of the effect of the ausforming temperature on the tempered martensitic microstructure in order to quantify the importance of ausforming in the TMT to optimize the creep strength. The conclusions achieved in this work will allow us to clarify what processing parameters affect the heterogeneous formation of thermally stable precipitates.

2. Materials and Methods

A commercial G91 FM steel supplied by CIEMAT (Madrid, Spain) in the form of a plate was used in this work. The nominal chemical composition of this steel is given in Table 1. This material was received after a heat treatment consisting of normalization at 1040 °C for 30 min followed by tempering at 730 °C for 1 h, both with air cooling to room temperature.

Table 1. Nominal composition in wt % of Grade 91 ferritic/martensitic steel.

Elements	C	Si	Mn	Cr	Mo	V	Nb	N	Fe
Wt %	0.1	0.4	0.4	9.0	1.0	0.2	0.07	0.038	balance

Thermodynamic calculations, used as guidelines to select the temperatures for the Thermomechanical Treatment (TMT), were performed with the Thermo-Calc® (Solna, Sweden) software based on the CALPHAD (Computer Coupling of Phase Diagrams and Thermo-chemistry) using the database TCFE8. The new TMT approach proposed in this work is shown schematically in Figure 1. Cylindrical samples with 10 mm length × 5 mm diameter were given 20% deformation at 0.1 s^{-1} in a Bähr DIL 805A/D plastodilatometer (TA Instruments, New Castle, DE, USA). The samples were heated at 5 °C/s and cooled at 50 °C/s.

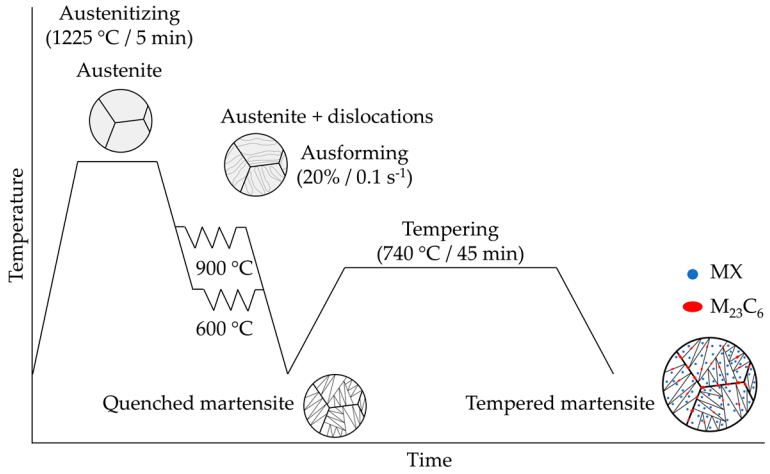

Figure 1. Thermomechanical Treatment (TMT) scheme.

The microstructure of as-received material and material after TMT simulation treatments was analyzed using optical microscopy, field emission gun scanning electron microscopy (FEG-SEM), orientation maps obtained by electron backscatter diffraction (EBSD), transmission electron microcopy (TEM), and X-ray diffraction (XRD). Standard grinding and polishing procedures were used for sample preparation, which included a final polish with 1 micron diamond paste. Polished specimens were

etched with a solution of 5 mL hydrochloric acid, 1 g of picric acid and 100 mL of ethyl alcohol (Vilella's reagent) to develop the microstructural features.

EBSD measurements were performed with a JEOL JSM 6500 FEG-SEM (JEOL Ltd., Tokyo, Japan) operating at 20 kV equipped with a fully automatic EBSD attachment from Oxford Instruments HKL (Abingdon, UK). Residual damage in EBSD samples from diamond polishing was removed through an additional polishing stage with colloidal (40 nm). EBSD mapping has been carried out on an area of about 900 × 400 μm^2 at step sizes of 0.4 μm. The HKL Channel 5 software (Oxford Instruments, Abingdon, UK) has been used for data processing in order to obtain a graphical representation of the microstructure by marking the sample points of the grains in a map using colors specific to the lattice orientation.

Observation of precipitates present in the microstructure was performed on thin foils by TEM in a JEOL JEM 2100 and a JEOL JEM 3000F (JEOL Ltd., Tokyo, Japan). For this goal, disks 3 mm in diameter and 100 μm in thickness were cut. The thickness of these slices were further mechanically thinned and, afterwards, twin-jet electropolishing was performed at 25 °C and 40 V using an electrolyte compose of 95% acetic acid and 5% percloric acid.

XRD studies were carried out with Co-K_α radiation in a Bruker AXS D8 diffractometer equipped with Goebel mirror optics and a LynxEye Linear Position Sensitive Detector for ultra-fast XRD measurements. For the Rietveld refinement of the diffractograms, the version 4.2 program TOPAS (4.2, Bruker AXS, Billerica, MA, USA) has been used and the crystallographic information of the phases used was obtained from Pearson's Crystal Structure Database for Inorganic Compounds, Release 2015/2016. Materials Park: ASM International, 2015. Line broadening due to the crystallite size and lattice strain was analyzed using the double-Voigt approach. It was concluded from this analysis that line broadening is mainly due to the microstrain produced by dislocations and their associated stress fields.

Finally, Vickers hardness measurements were performed with a load of 5 kg on the longitudinal section of warm/hot compressed material before and after tempering.

3. Results and Discussion

3.1. Thermodynamic Calculations

The equilibrium phase mole fraction of the coexisting phases in the microstructure of the G91 FM steel is shown in Figure 2 as a function of temperature. According to this figure, $M_{23}C_6$ carbides will dissolve during the conventional austenitizing treatment at 1040 °C, remaining undissolved about 1.59×10^{-3} mole fraction of MX precipitates. In order to improve the creep strength during the service life, it is necessary to maximize the amount of MX carbides finely dispersed that precipitate during the TMT. This point emphasizes the importance of increasing the austenitizing temperature to guarantee the dissolution of most MX precipitates present in the as-received microstructure. However, this treatment must be performed in the fully austenite region to avoid the presence of δ-ferrite, which is generally regarded as detrimental for creep properties [19]. Since δ-ferrite forms above 1255 °C, according to Figure 2, an austenitizing temperature of 1225 °C was selected. At this temperature, 5 min treatment was enough to get a complete homogenization of the microstructure due to the small size of the sample used. The effect of increasing the austenitizing temperature on the precipitation reactions during tempering was evaluated using Thermo-Calc®. The volume fraction of MX carbides (with M = Nb, V and X = C, N) present in the austenite decreases from 1.32×10^{-3} to 1.01×10^{-4} when the temperature is increased from 1040 to 1225 °C. Therefore, more Nb/V/C/N will be available in solid solution in the austenite at 1225 °C, compared to 1040 °C, to precipitate during the subsequent tempering step. Thus, as some MX precipitates will still remain undissolved after austenitizing, the composition (of the martensite) prior to the calculation at the tempering step has to be corrected. These calculations show an increase in the volume fraction of MX precipitates during tempering at 740 °C from 1.42×10^{-3} to 2.67×10^{-3} when the austenitizing temperature is increased from 1040

to 1225 °C (two times greater). It should be kept in mind when comparing these calculations to the experimental results that the authors assumed that quasi-equilibrium has been reached during the austenitizing and tempering steps investigated in this work.

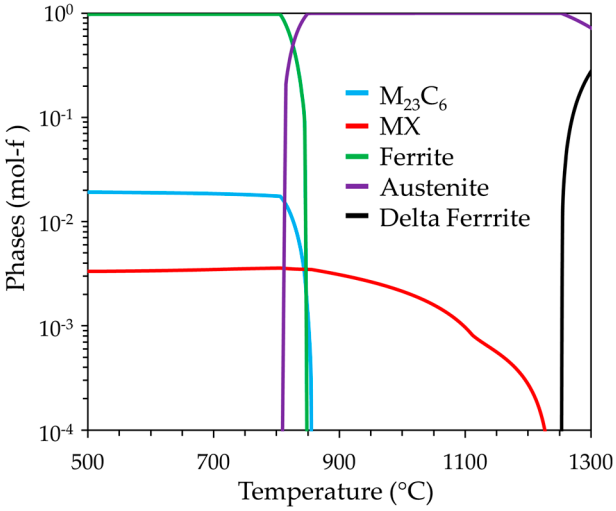

Figure 2. Temperature evolution of phase mole fraction in G91 calculated by ThermoCalc.

3.2. Microstructural Characterization

As shown in the micrograph of Figure 3a, as-received G91 steel presents a tempered martensite microstructure, with grain and lath boundaries decorated by tiny bright spots corresponding to $M_{23}C_6$ particles precipitated during tempering. Quantitative metallography studies revealed an average lath size ranging from 0.25 to 0.5 µm [20]. Examination of this microstructure at higher magnifications with a TEM reveals the presence of MX precipitates, distributed in the matrix within the lath, in addition to $M_{23}C_6$, distributed only on boundaries. As shown in Figure 3b,c, the size of these precipitates ranges from 100 to 200 nm for $M_{23}C_6$ carbides and from 20 to 50 nm for MX precipitates.

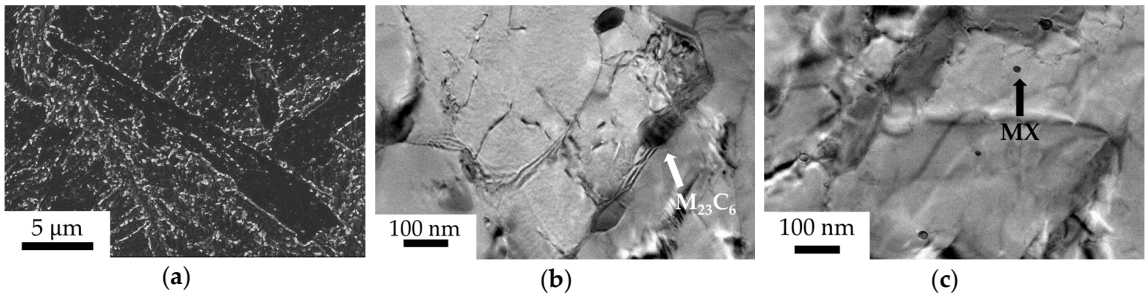

Figure 3. Microstructure of G91 after conventional heat treatment showing $M_{23}C_6$ precipitates (**a**) on grain boundaries (Scanning electron microscopy (SEM) micrograph) and (**b**) on lath boundaries (Transmission electron microcopy (TEM) micrograph) and (**c**) MX within laths (TEM micrograph).

SEM examination showed that, during the austenitizing treatment at 1225 °C, all carbides were dissolved except for a negligible volume fraction of Nb rich MX precipitates (Figure 4).

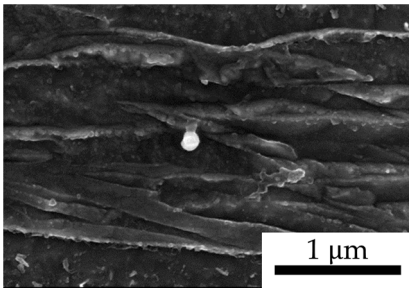

Figure 4. SEM micrographs showing Nb rich MX precipitate after austenitizing treatment at 1225 °C.

The XRD pattern obtained in a sample quenched to room temperature after the austenitization showed only the diffraction peaks of ferrite (Figure 5). No retained austenite was detected in the microstructure by this technique after the austenitization heat treatment.

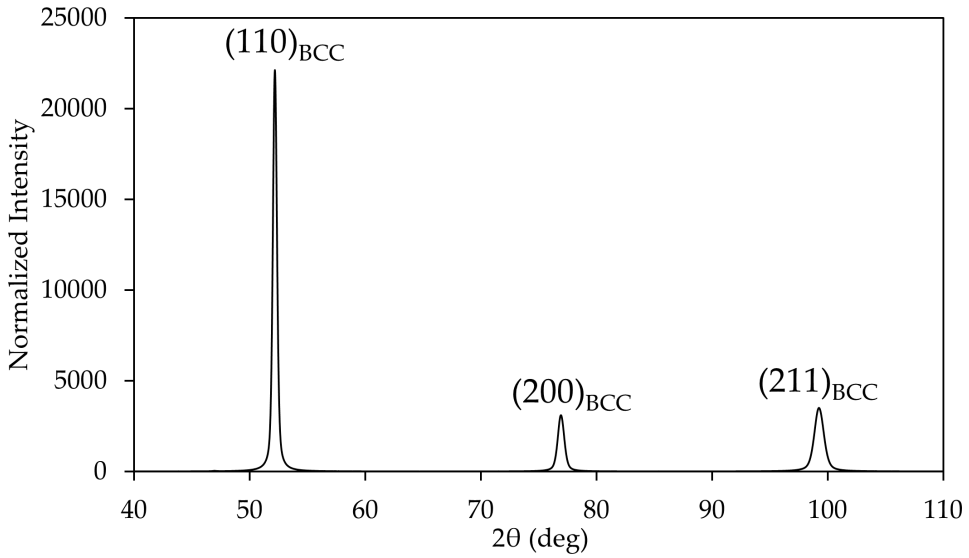

Figure 5. X-ray diffraction pattern after austenitizing at 1225 °C. BCC stands for body-centered cubic ferrite.

Comparing the average prior austenite grain size present in as-received material (43 µm) and after austenitizing at 1225 °C (259 µm), it is observed that a considerable grain growth occurs (Figure 6). No δ-ferrite has been formed after austenitizing at 1225 °C. The inhibition of the austenite grain growth during austenitizing is related to the presence of fine second phase particles, dispersed in the microstructure, that pin the grain boundaries and restrain their movement. The explosive growth observed indicates that around 1225 °C most of the MX and $M_{23}C_6$ precipitates are dissolved. In general, a coarse-grained microstructure presents better creep properties. High-temperature creep is controlled by diffusion, and thus creep strength increases with a decreasing the amount of regions with a high diffusion rate like grain boundaries.

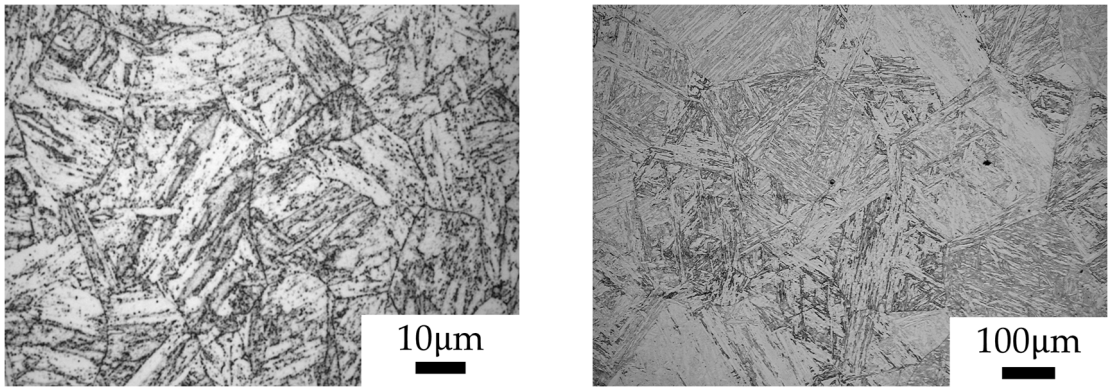

Figure 6. Optical micrographs showing the prior austenite grain microstructure in G91: (**a**) after conventional heat treatment and (**b**) after austenitizing at 1225 °C.

To maximize the number of nanoscale MX precipitates, a thermomechanical procedure was used to increase the dislocation density in the steel, increasing the number of nucleation sites for precipitation inside the martensite laths during the subsequent tempering stage at 740 °C. After austenitizing at 1225 °C, samples were cooled to either 900 or 600 °C and hot-worked in a controlled manner. Hot deformation at 900 °C results in dynamic recrystallization (DRX) as can be seen in Figure 7, leading to grain refinement, from 259 µm for austenitized at 1225 °C material to 141 µm. On the other hand, as the transformation of austenite to ferrite at 600 °C would take place after a long time, metastable austenite can be plastically deformed at this temperature without inducing this phase transformation. In this case, the low ausforming temperature and high strain rate would suggest that neither recrystallization nor recovery of the microstructure is taking place and, thus, a more refined martensitic structure in the quenched samples is expected.

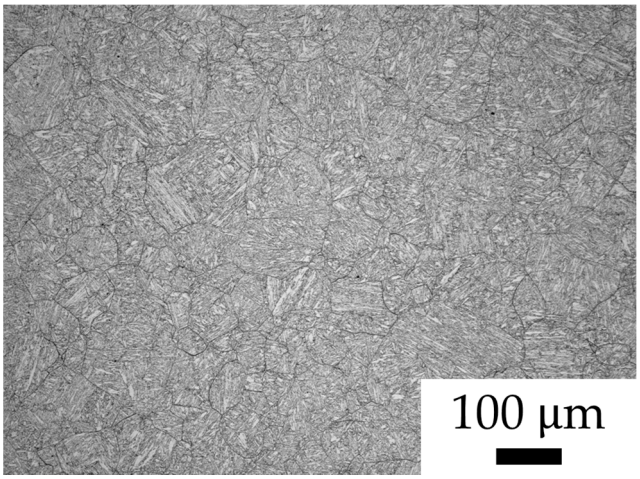

Figure 7. Optical micrographs showing the prior austenite grain microstructure in G91 after ausfroming at 900 °C.

EBSD investigations revealed a significant difference in the substructure of the samples ausformed at 600 and 900 °C, as shown in Figure 8a,b, respectively. While samples deformed at 900 °C showed the typical lath martensite structure of blocks (Figure 8b), this lath-like morphology after deformation at 600 °C is blurred (Figure 8a). This is attributed to the higher number density of dislocations introduced during the deformation of austenite at 600 °C, which hindered typical block growth during the martensitic transformation. Table 2 collects the block width measured on three IPF (Inverse pole

figure) maps obtained by EBSD for each sample by the linear intercept method [21]. Boundaries with a misorientation larger than 10 were considered as block boundaries in the measurements. Our observations reveal coarser blocks at the lower ausforming temperature. This is consistent with the variant selection concept reported by other authors [22,23], where the strengthening of austenite enhances self-accommodation of the transformation strain by formation of preferential variants. Compared to the G91 in as-received condition (Figure 8c), whose values were also measured (Table 2), a higher block width is obtained for the samples after TMT due to the higher austenitization temperature used in the TMT.

Table 2 shows the lath width measured on eight TEM micrographs for each microstructures by the linear intercept method. These results demonstrate that the lath width in the G91 in as-received conditions can be refined by TMT, and that the decrease of the ausforming temperature leads to a decrease of the martensite lath width. This fact is easily explainable because the lath width depends on the strength of austenite and, thus, lower ausforming temperatures enable greater austenite strengthening [24].

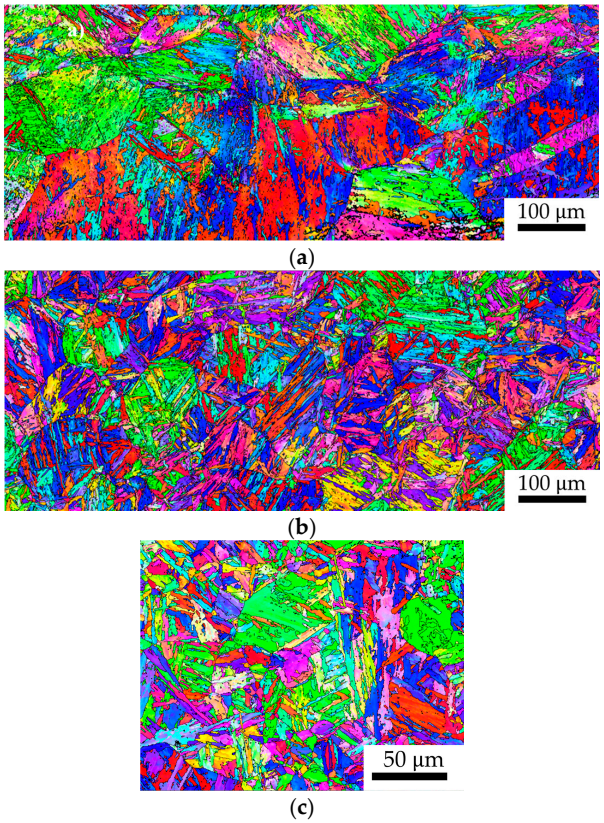

Figure 8. IPF (Inverse pole figure) maps after TMT for the sample (**a**) ausformed at 600 °C, (**b**) ausformed at 900 °C, (**c**) G91 in as-received condition

Table 2. Block and lath width for the samples after TMT and G91 in as-received condition.

Sample	Block Width (µm)	Lath Width (nm)
G91 as-received	2.71 ± 0.23	356 ± 35
Def. at 900 °C	3.23 ± 0.26	285 ± 26
Def. at 600 °C	3.91 ± 0.36	212 ± 59

Table 3 shows that hardness of as-quenched sample is increased by the ausforming treatment. The higher hardness value obtained for the sample ausformed at 600 °C could be justified on the basis

of having a higher dislocation density and a finer martensite lath-structure, which is related to the lack of dynamic recrystallization during ausforming at 600 °C.

Table 3. Hardness values after austenitization and ausforming at different temperatures.

No Def.	Def. at 900 °C	Def. at 600 °C
426 ± 3	434 ± 5	465 ± 10

As shown in Table 4, ausforming causes a decrease in the martensite start (Ms) and finish (Mf) temperatures, resulting from the mechanical stabilization of austenite produced when the strength of austenite is enough to avoid the motion of glissile interfaces [25]. Therefore, the higher dislocation density obtained for the sample ausformed at 600 °C is translated into having the lowest transformation temperature.

Table 4. Martensitic transformation temperatures after austenitization and ausforming at different temperatures and quenching (50 °C/s) to room temperature.

Sample	Ms (°C)	Mf (°C)	ΔM (°C)
Austenitized	385	220	165
Def. at 900 °C	374	195	179
Def. at 600 °C	338	145	193

Tempering is the key step of the TMT to achieve the optimum precipitate size, and the recovery degree of the martensitic matrix that guarantees the optimal combination of toughness and creep strength properties. As commercially used for this steel grade, a tempering temperature of 740 °C and a holding time of 45 min were selected in this work. To understand the effect of the TMT applied, the number density and average size of precipitates were calculated analyzing at least 100 precipitates for MX from TEM micrographs and 300 $M_{23}C_6$ from SEM micrographs. As shown in Table 5, the ausforming treatment does not produce a significant change in size and distribution of the $M_{23}C_6$. The precipitation processes of these carbides take place on prior austenite grain, block, and lath boundaries as soon as the tempering begins, and it is completed in a short time [26] (Figure 9a,b,d,e). The lath refinement produced during ausforming can increase the number of potential nucleation sites for these precipitates on lath boundaries. By contrast, greater block width and prior austenite grain is obtained after TMT. Since $M_{23}C_6$ precipitates nucleate first on prior austenite grain and block boundaries due to its higher energy, the remaining carbon content will precipitate as $M_{23}C_6$ on lath boundaries obtaining finer $M_{23}C_6$ distribution in TMT samples. This difference in size between the $M_{23}C_6$ formed on lath boundaries, and those nucleated on block and prior austenite grain boundaries, may produce a faster Ostwald ripening coarsening resulting in an average $M_{23}C_6$ size and number density similar to the G91 in as-received condition. Besides, the number density of MX precipitates in the TMT samples increases in three orders of magnitude, having a size about four times smaller than those in the G91 in as-received condition, which is in good agreement with previous works where similar thermomechanical treatment were applied in G91 [8,14] (Figure 9c,f). The higher austenitization temperature and ausforming processing greatly increased the dislocation density in austenite as others author have demonstrated in previous works [27], resulting in a higher number of nucleation sites for precipitation of MX precipitates inside the martensite laths. Thus, the higher dislocation density introduced by deformation at 600 °C is responsible for a smaller size of these precipitates and the slightly higher number density. Partial recrystallization during ausforming at 900 °C causes a significant decrease in dislocation density in recrystallized grains as well as an inhomogeneous distribution of MX precipitate.

Table 5. Number density and size of precipitates after TMT and G91 in as-received condition.

Sample	Precipitate	Diameter (nm)	Number Density (m^{-3})
G91 as-received	$M_{23}C_6$ MX	141 ± 4 25 ± 0.6	6.20^{19} 8.1410^{19}
Def. at 900 °C	$M_{23}C_6$ MX	125 ± 3 7.4 ± 0.3	8.5010^{19} 6.410^{22}
Def. at 600 °C	$M_{23}C_6$ MX	136 ± 5 5.59 ± 0.4	3.7810^{19} 9.3910^{22}

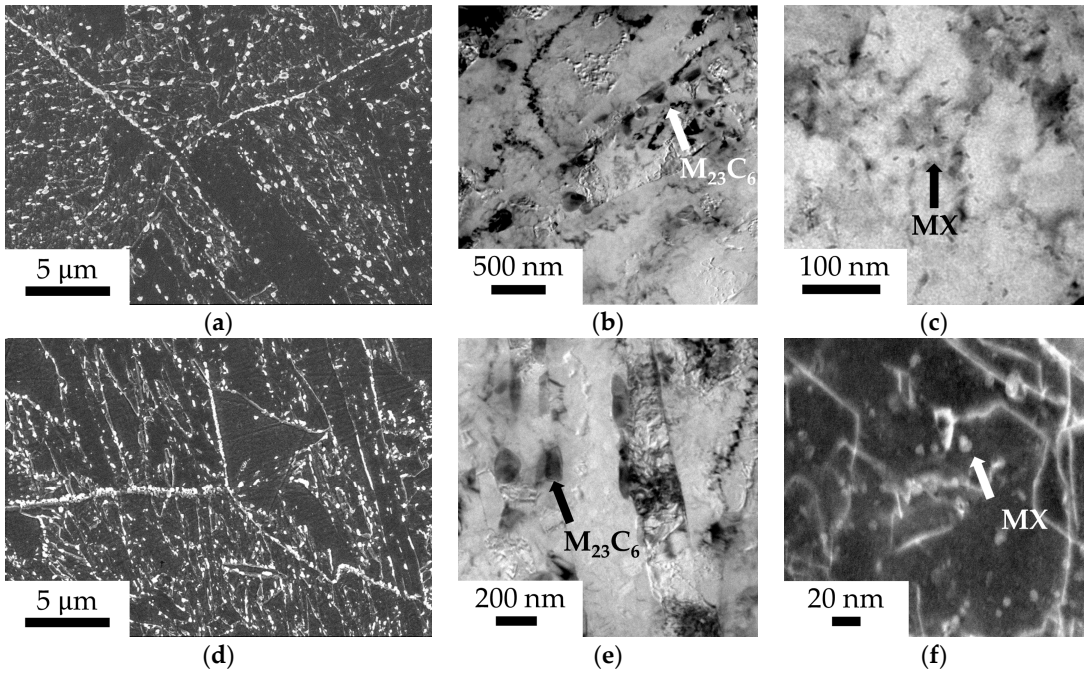

Figure 9. (**a**) SEM micrograph showing $M_{23}C_6$ on grain boundaries and TEM micrographs showing, (**b**) $M_{23}C_6$ on lath boundaries, and (**c**) MX within laths for the sample after TMT (ausformed at 600 °C); and (**d**) SEM micrograph and TEM micrographs showing (**e**) $M_{23}C_6$ on lath boundaries and (**f**) MX within laths for the sample after TMT (ausformed at 900 °C).

Hardness measurements were performed in the G91 in as-received condition and after TMTs (Table 6). The samples after TMTs show hardness values up to 50 HV5 higher than the ones for G91 in as-received condition, being the values for the TMT samples very similar. These results together with the microstructural characterization carried out demonstrate the improvement in strength after TMT, which is attributable to the lath refinement along with the increase in number density and reduction in size of MX precipitates.

Table 6. Hardness values for the sample after TMT and G91 in as-received condition.

G91 as-Received	Def. at 900 °C	Def. at 600 °C
260 ± 2	310 ± 9	307 ± 8

4. Conclusions

The microstructural analyses carried out allow us to conclude that applying a TMT instead of conventional heat treatment on G91 ferritic/martensitic steel will promote:

1. Microstructures containing three orders of magnitude higher number density and four times smaller size of MX precipitates.
2. Microstructures contain $M_{23}C_6$ precipitates with very similar values of size and number density.
3. An increase in hardness of 50 HV5, which is attributable to the increase in the number density and the reduction in the size of MX nanoprecipitates and the lath width refinement.

The main conclusions reached on the effect of ausforming on the martensitic microstructure are summarized below:

4. The martensitic microstructure reduces its lath width due to the strengthening of austenite produced by ausforming. However, ausforming at 600 °C results in a higher block width as compared to ausfoming at 900 °C because of the variant selection that takes place during the martensitic transformation in the sample ausformed at 600 °C.
5. The ausforming temperature does not affect $M_{23}C_6$ distribution and size, but ausforming at 600 °C leads to a slightly smaller size of MX.

Acknowledgments: The authors acknowledge financial support to Spanish Ministerio de Economia y Competitividad (MINECO) in the form of a Coordinate Project (MAT2016-80875-C3-1-R). The work presented here is done within the Joint Program on Nuclear Materials of the European Energy Research Alliance Pilot Project CREMAR. The authors also would like to acknowledge financial support to Comunidad de Madrid through DIMMAT-CM_S2013/MIT-2775 project. The authors are grateful to Javier Vara, Alberto Delgado, and Alberto López for the experimental support. Javier Vivas acknowledges financial support in the form of a FPI Grant BES-2014-069863.

Author Contributions: All authors were involved in discussing the results and in finalizing the manuscript.

Conflicts of Interest: The authors declare no conflict of interest.

References

1. Mayer, K.H.; Masuyama, F. The development of creep-resistant steels. In *Creep-Resistant Steels*; Woodhead Publishing: Cambridge, UK, 2008; pp. 15–77.
2. Klueh, R.L.; Gelles, D.S.; Jitsukawa, S.; Kimura, A.; Odette, G.R.; van der Schaaf, B.; Victoria, M. Ferritic/martensitic steels—Overview of recent results. *J. Nucl. Mater.* **2002**, *307*, 455–465. [CrossRef]
3. Klueh, R.L.; Ehrlich, K.; Abe, F. Ferritic/martensitic steels: Promises and problems. *J. Nucl. Mater.* **1992**, *191*, 116–124.
4. Helis, L.; Toda, Y.; Hara, T.; Miyazaki, H.; Abe, F. Effect of cobalt on the microstructure of tempered martensitic 9Cr steel for ultra-supercritical power plants. *Mater. Sci. Eng. A* **2009**, *510*, 88–94. [CrossRef]
5. Kipelova, A.; Kaibyshev, R.; Belyakov, A.; Molodov, D. Microstructure evolution in a 3% co modified P911 heat resistant steel under tempering and creep conditions. *Mater. Sci. Eng. A* **2011**, *528*, 1280–1286. [CrossRef]
6. Knežević, V.; Balun, J.; Sauthoff, G.; Inden, G.; Schneider, A. Design of martensitic/ferritic heat-resistant steels for application at 650 °C with supporting thermodynamic modelling. *Mater. Sci. Eng. A* **2008**, *477*, 334–343. [CrossRef]
7. Rojas, D.; Garcia, J.; Prat, O.; Sauthoff, G.; Kaysser-Pyzalla, A.R. 9%Cr heat resistant steels: Alloy design, microstructure evolution and creep response at 650 °C. *Mater. Sci. Eng. A* **2011**, *528*, 5164–5176. [CrossRef]
8. Klueh, R.L.; Hashimoto, N.; Maziasz, P.J. Development of new nano-particle-strengthened martensitic steels. *Scr. Mater.* **2005**, *53*, 275–280. [CrossRef]
9. Hollner, S.; Fournier, B.; Le Pendu, J.; Cozzika, T.; Tournié, I.; Brachet, J.C.; Pineau, A. High-temperature mechanical properties improvement on modified 9Cr–1mo martensitic steel through thermomechanical treatments. *J. Nucl. Mater.* **2010**, *405*, 101–108. [CrossRef]
10. Tan, L.; Busby, J.T.; Maziasz, P.J.; Yamamoto, Y. Effect of thermomechanical treatment on 9Cr ferritic–martensitic steels. *J. Nucl. Mater.* **2013**, *441*, 713–717. [CrossRef]
11. Hollner, S.; Piozin, E.; Mayr, P.; Caës, C.; Tournié, I.; Pineau, A.; Fournier, B. Characterization of a boron alloyed 9Cr3W3CoVNbBN steel and further improvement of its high-temperature mechanical properties by thermomechanical treatments. *J. Nucl. Mater.* **2013**, *441*, 15–23. [CrossRef]

12. Abe, F. Precipitate design for creep strengthening of 9% Cr tempered martensitic steel for ultra-supercritical power plants. *Sci. Technol. Adv. Mater.* **2008**, *9*, 013002. [CrossRef] [PubMed]
13. Maruyama, K.; Sawada, K.; Koike, J.I. Strengthening mechanisms of creep resistant tempered martensitic steel. *ISIJ Int.* **2001**, *41*, 641–653. [CrossRef]
14. Klueh, R.L.; Hashimoto, N.; Maziasz, P.J. New nano-particle-strengthened ferritic/martensitic steels by conventional thermo-mechanical treatment. *J. Nucl. Mater.* **2007**, *367*, 48–53. [CrossRef]
15. Li, S.; Eliniyaz, Z.; Sun, F.; Shen, Y.; Zhang, L.; Shan, A. Effect of thermo-mechanical treatment on microstructure and mechanical properties of p92 heat resistant steel. *Mater. Sci. Eng. A* **2013**, *559*, 882–888. [CrossRef]
16. Abe, F. Coarsening behavior of lath and its effect on creep rates in tempered martensitic 9Cr-W steels. *Mater. Sci. Eng. A* **2004**, *387*, 565–569. [CrossRef]
17. Tamura, M.; Sakasegawa, H.; Kohyama, A.; Esaka, H.; Shinozuka, K. Effect of mx type particles on creep strength of ferritic steel. *J. Nucl. Mater.* **2003**, *321*, 288–293. [CrossRef]
18. Tan, L.; Byun, T.S.; Katoh, Y.; Snead, L.L. Stability of mx-type strengthening nanoprecipitates in ferritic steels under thermal aging, stress and ion irradiation. *Acta Mater.* **2014**, *71*, 11–19. [CrossRef]
19. Kimura, K.; Sawada, K.; Kushima, H.; Toda, Y. Influence of chemical composition and heat treatment on long-term creep strength of grade 91 steel. *Procedia Eng.* **2013**, *55*, 2–9. [CrossRef]
20. Klueh, R.L. Elevated temperature ferritic and martensitic steels and their application to future nuclear reactors. *Int. Mater. Rev.* **2005**, *50*, 287–310. [CrossRef]
21. Caballero, F.G.; Roelofs, H.; Hasler, S.; Capdevila, C.; Chao, J.; Cornide, J.; Garcia-Mateo, C. Influence of bainite morphology on impact toughness of continuously cooled cementite free bainitic steels. *Mater. Sci. Technol.* **2012**, *28*, 95–102. [CrossRef]
22. Shi, Z.; liu, K.; Wang, M.; Shi, J.; Dong, H.; Pu, J.; Chi, B.; Zhang, Y.; Jian, L. Effect of tensile deformation of austenite on the morphology and strength of lath martensite. *Met. Mater. Int.* **2012**, *18*, 317–320. [CrossRef]
23. Miyamoto, G.; Iwata, N.; Takayama, N.; Furuhara, T. Variant selection of lath martensite and bainite transformation in low carbon steel by ausforming. *J. Alloys Compd.* **2013**, *577*, S528–S532. [CrossRef]
24. Zhang, M.; Wang, Y.H.; Zheng, C.L.; Zhang, F.C.; Wang, T.S. Austenite deformation behavior and the effect of ausforming process on martensite starting temperature and ausformed martensite microstructure in medium-carbon si–al-rich alloy steel. *Mater. Sci. Eng. A* **2014**, *596*, 9–14. [CrossRef]
25. Chatterjee, S.; Wang, H.S.; Yang, J.R.; Bhadeshia, H.K.D.H. Mechanical stabilisation of austenite. *Mater. Sci. Technol.* **2006**, *22*, 641–644. [CrossRef]
26. Prat, O.; García, J.; Rojas, D.; Sanhueza, J.P.; Camurri, C. Study of nucleation, growth and coarsening of precipitates in a novel 9%Cr heat resistant steel: Experimental and modeling. *Mater. Chem. Phys.* **2014**, *143*, 754–764. [CrossRef]
27. Seo, S.W.; Jung, G.S.; Lee, J.S.; Bae, C.M.; Bhadeshia, H.K.D.H.; Suh, D.W. Ausforming of medium carbon steel. *Mater. Sci. Technol.* **2015**, *31*, 436–442. [CrossRef]